Thermal Management System Architecture for the Powertrain of a 90-Seater Battery-Electric Aircraft

Giuffré, A.; de Vries, Reynard ; Wolleswinkel, Rob E. ; de Servi, C.M.

Important note
To cite this publication, please use the final published version (if applicable).
Please check the document version above.

AIAA Aviation Forum and ASCEND co-located Conference Proceedings
21 - 25 July 2025, Las Vegas, Nevada
AIAA AVIATION FORUM AND ASCEND 2025

10.2514/6.2025-3207

Thermal Management System Architecture for the Powertrain of a 90-Seater Battery-Electric Aircraft

Andrea Giuffré*, Reynard de Vries[†], Rob E. Wolleswinkel[‡],
Elysian Aircraft, Rendementsweg 2, 3641SK Mijdrecht, The Netherlands

Carlo M. De Servi[§]
Delft University of Technology, Kluyverweg 1, 2629HS Delft, The Netherlands

The preliminary design of the thermal management system for the electric powertrain of a 90-seater battery-electric aircraft is addressed in this study. The main heat loads of the powertrain are associated with the battery pack and the electronic power unit, comprising an electric motor, an inverter, and optionally a gearbox. The main operating points of the thermal management system throughout the nominal flight mission are identified as take-off, top of climb, cruise, and top of descent. Two candidate architectures are assessed and compared in terms of key performance metrics, i.e., weight, drag penalty, and electric power consumption. Moreover, the equivalent battery mass required to power and carry the thermal management system throughout the flight mission is computed. The results show that the architecture exploiting the difference in the temperature levels of the heat sources in the powertrain features superior performance than the baseline configuration. In particular, the total equivalent battery mass is reduced by 388 kg. Overall, this translates into an increase in the usable range of 11 km prior to snowball effects, highlighting the importance of the thermal management system in the design of large battery-electric aircraft.

I. Nomenclature

CR	=	Cruise
EM	=	Energy mass [kg]
EPU	=	Electronic power unit
eVTOL	=	Electrical vertical take-off and landing
GWP	=	Global warming potential
ISA	=	International standard atmosphere
MTOM	=	Maximum take-off mass [kg]
PMAD	=	Power management and distribution system
TMS	=	Thermal management system
TO	=	Take-off
TOC	=	Top of climb
TOD	=	Top of descent
VCC	=	Vapor compression cycle
A	=	Area [m^2]
C_D	=	Drag coefficient [-]
C_p	=	Pressure recovery factor [-]
D	=	Drag force [N]
e	=	Gravimetric energy density [J kg^{-1}]
h	=	Altitude [m]
L	=	Lift force [N]
M	=	Mach number [-]
$\dot{m}$	=	Mass flow rate [kg s^{-1}]
P	=	Pressure [Pa] - power [W]
$\dot{Q}$	=	Heat flow rate [W]
T	=	Temperature [K] - thrust force [N]
V	=	Volume [m^3]
v	=	Velocity [m s^{-1}]
β	=	Pressure ratio [-]
η	=	Efficiency [-]
ρ	=	Density [kg m^{-3}]
θ	=	Inclination angle [rad]

---

*Senior Thermal Engineer, andrea@elysianaircraft.com, AIAA member
[†]Chief Engineer, reynard@elysianaircraft.com, Senior AIAA member
[‡]Co-CEO and CTO, rob@elysianaircraft.com, Senior AIAA member
[§]Senior Researcher, Propulsion & Power, c.m.deservi@tudelft.nl

II. Introduction

In 2022 the aviation sector accounted for 1.9% of global greenhouse gas emissions, 2.5% of global CO_2 emissions, and 3.5% of effective radiative forcing [1]. The incremental improvements in fuel efficiency of conventional aircraft are currently insufficient to offset the increasing passenger demand while complying with the sustainability goals set by, e.g., the European Commission in the Flightpath 2050 [2, 3]. Therefore, revolutionary aircraft concepts featuring electrified propulsion systems are needed to reach the long-term target of net zero emissions. In this context, battery-electric propulsion is commonly deemed as an unsuitable pathway for large passenger aircraft when relying on current and near-future battery technology, i.e., 200-500 Wh/kg [4–7]. However, a recent study challenged the belief that battery-electric propulsion might be used only for small commuter aircraft flying over short distances, by highlighting four common misconceptions in the scientific literature [8]. Based on such considerations, a follow-up study demonstrated that it is theoretically possible to design a 90-seater battery-powered aircraft with a useful range of 800 km for a pack-level energy density of 360 Wh/kg [9]. The resulting aircraft has an estimated energy consumption of 167 Wh/pax-km, leading to approximately 70-80% lower grid energy consumption than eSAF-based alternatives, and 40% to 75% less than hydrogen-based alternatives [9]. However, the aircraft conceptual design has been performed with class-II design methods [10, 11] and is based on several system-level assumptions. To verify the validity of such assumptions, further research has been performed in ten key technical areas. This work documents the research efforts focused on the Thermal Management System (TMS) for the electric powertrain, comprising battery pack, electric motors, inverters, and optionally gearbox. Additional heat loads associated with the avionics, Power Management And Distribution (PMAD) system, ice protection system, environmental control of the cabin and cockpit, and gas turbine-based reserve energy system are disregarded in this study.

The conceptual design of the TMS for the powertrain of hybrid-electric aircraft has been already addressed in previous studies. In [12] the authors provided an assessment of various TMS architectures, by comparing key performance metrics, such as weight, volume, electric power consumption, and ram air flow requirements. The study is useful to identify the most promising technologies, but it does not provide any information regarding the design of the TMS for a specific aircraft configuration. Rheaume et al. investigated the impact of the TMS on the fuel consumption of a 5 MW parallel hybrid configuration for a commercial, single-aisle aircraft. In their first study, the battery pack and the motor drive share the same ram air-cooled liquid loop operating with a 50% mixture of water and propylene glycol, whereas the engine and gearbox are cooled by an oil loop operating with MIL-PRF-23699, i.e., a synthetic oil commonly used for aviation applications [13]. For the prescribed configuration, the impact of the TMS on the total fuel burn evaluated throughout the nominal flight mission is approximately 3.4%. In a follow-up study, the authors modified the TMS architecture by separating the coolant loops of the battery pack and the motor drive, thus allowing the latter to operate at a higher temperature, leading to a downsizing of the correspondent heat exchanger. Moreover, the authors proposed to pre-cool the battery pack before take-off to leverage its thermal inertia and postpone the activation of the onboard TMS until the mid-climb phase. Overall, the total fuel consumption of the TMS has been reduced to approximately 0.7% [14]. In [15] the authors evaluated the performance of a ram air-based TMS throughout the flight envelope of a 180-seater partial turbo-electric aircraft. The study addressed the heat loads associated with electric motors, generators, and power electronics. The prescribed sizing point of the TMS was top of climb, whereas the most critical operating point was identified as take-off during a hot day. In such conditions, the authors suggested the use of a puller fan in the ram air duct to avoid TMS oversizing. In an additional parametric study performed by Planès et al. [16], the performance of a ram air-cooled liquid loop has been compared to the one of a Vapor Compression Cycle (VCC). The case studies under analysis were a single-aisle passenger aircraft and a business jet, featuring a more elctric aircraft architecture. The selected operating point was cruise flight at ISA conditions. The authors concluded that a VCC architecture featuring flush ram air intakes consistently leads to superior performance than a liquid loop using ram air as heat sink.

Differently from the aforementioned studies, the present work is focused on an electric aircraft flying the nominal mission purely on battery power. For such configuration, the TMS has a larger impact on the weight, drag penalty, and electric power consumption at aircraft level, thus its optimization has a direct influence on the usable range. To properly assess such impact, this work features a model-based system engineering approach integrating the conceptual design of the TMS with the preliminary design of its main components. Moreover, the present study documents a comparison between a baseline architecture and an alternative configuration exploiting potential synergies among the heat loads associated with the various components of the electric powertrain. The remainder of the paper is structured as follows. The selected aircraft configuration, the flight mission, and the operating envelope of the TMS are described in Sec. III. The baseline and alternative system architectures are introduced in Sec. IV. The methodology is documented in Sec. V, with particular emphasis on the models of the main components. The results are presented in Sec. VI and the main takeaways are summarized in Sec. VII.
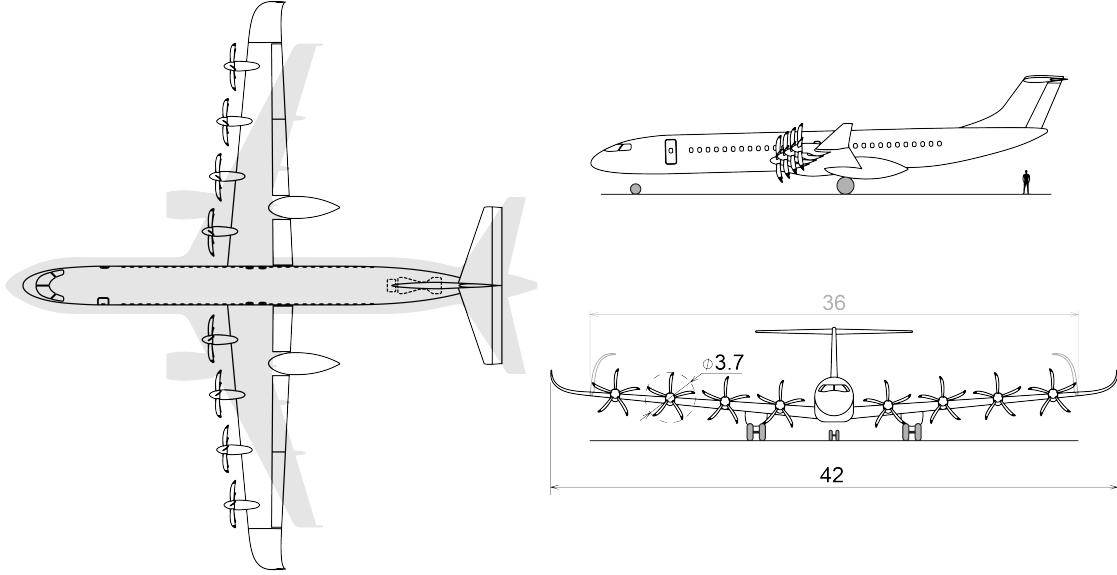
2

Fig. 1 Three-views drawing of a 90-seater, battery-electric passenger aircraft with a gas-turbine-based reserve energy system displayed with dotted lines. The A320 planform is included in the top view for scale. Dimensions are reported in meters. Figure adapted from [9].

Table 1 Overview of main design parameters of the 90-seater battery-powered aircraft documented in [9].

Parameter	Value	Parameter	Value
Maximum take-off mass MTOM	76,000 kg	Maximum lift-to-drag ratio $(L/D)_{max}$	23
Energy mass EM	34,930 kg	Efficiency of battery η_{bat}	0.95
Pack-level energy density e_{bat}	360 Wh/kg	Efficiency of PMAD η_{pmad}	0.96
Usable energy density e_{us}	324 Wh/kg	Propulsive efficiency η_p	0.87

III. Case Study

The vehicle under analysis is the 90-seater battery-powered aircraft described in [9]. The layout is schematically displayed in Fig. 1, and the main aircraft design parameters used in the remainder of this work are summarized in Tab. 1. The aircraft features a tube-and-wing design with eight distributed propellers and a gas-turbine-based reserve energy system. Therefore, it is technically a hybrid-electric aircraft, although the nominal mission is flown purely on battery power, and the fuel-based reserve energy system is activated only for emergencies. Each Electronic Power Unit (EPU) is constituted by an electric motor, an inverter, and it may optionally feature a gearbox. On the one hand, the use of a gearbox decouples the propeller shaft from the motor drive, thus enabling the optimization of the motor rotational speed independently from the propeller rotational speed, leading to lower losses and lower heat load. On the other hand, the gearbox itself requires active cooling, thus introducing an additional heat load. Therefore, the presence or the absence of a gearbox leads to marginal changes in the EPU cooling requirements. For conciseness, only the direct-drive EPU configuration is analyzed in this work. The battery pack is located in the wingbox and is electrically connected to the EPUs via the power management and distribution system. For the purpose of this study, the battery is topologically split into eight packs, i.e., one for each EPU, featuring the same heat capacity of approximately 4366 kJ/K.

The flight mission is shown in Fig. 2, together with the average C-rate and battery state of charge associated with each segment [17]. The operating points characterized by the highest EPU power setting and the highest battery discharge rate, thus also the highest heat loads, are Take-Off (TO) and go-around. From the TMS perspective, the go-around procedure is slightly less critical than TO, as the initial temperature of the battery pack and the EPUs is lower at the end of the descent phase than at the end of taxiing. As suggested in [18], the TMS cooling requirements during TO and the
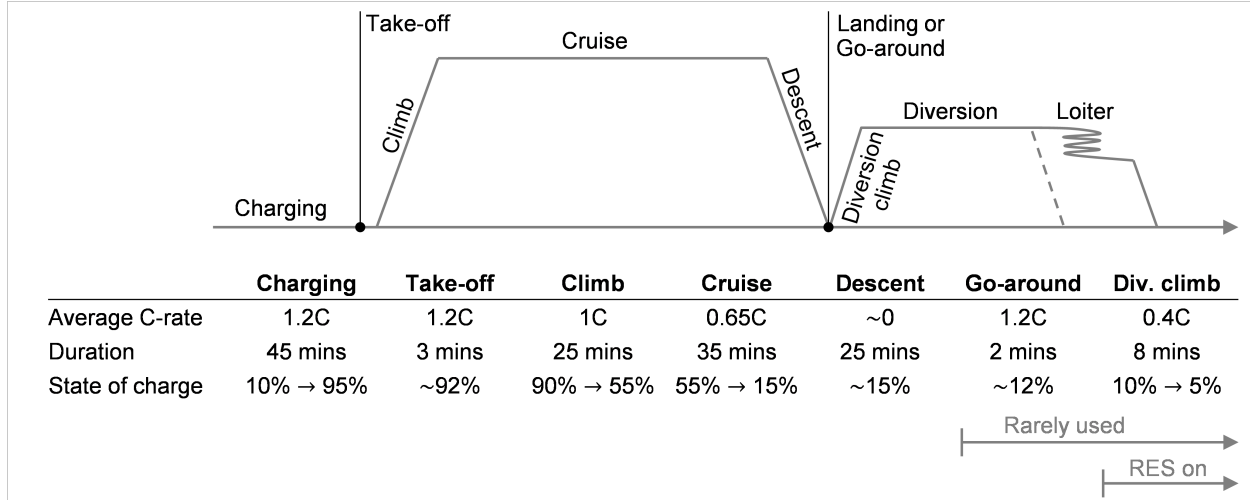
3

Fig. 2 **Average (dis)charge rates and corresponding states of charge for different mission segments throughout the flight mission, including reserves. Figure adapted from [17].**

Table 2 **Operating points selected to size and assess the performance of the TMS throughout the nominal flight mission. The values of heat loads refer to the entire electric powertrain, i.e., eight EPUs and eight battery packs.**

Operating Point	$\dot{Q}_{bat}$ [kW]	$\dot{Q}_{epu}$ [kW]	M_∞ [−]	h [km]	P_{amb} [kPa]	T_{amb} [°C]
TO ISA	300	635	0.2	0	101.3	15
TOC ISA	500	528	0.565	7.62	37.6	-34.5
CR ISA	450	324	0.565	7.62	37.6	-34.5
TOD ISA	400	324	0.565	7.62	37.6	-34.5
TO ISA+35	315	667	0.2	0	101.3	50
TOC ISA+35	525	554	0.565	7.62	37.6	0.5
CR ISA+35	472.5	340	0.565	7.62	37.6	0.5
TOD ISA+35	420	340	0.565	7.62	37.6	0.5

initial climb phase could be reduced by exploiting the thermal inertia of the battery pack. This could be achieved by pre-cooling the battery pack before TO at a set point below the maximum nominal operating temperature, e.g., 30°C for lithium-ion batteries. Expanding on this concept, the TMS cooling power could be modulated during the climb phase to achieve the maximum nominal operating temperature of the battery pack, e.g., 45°C, at Top Of Climb (TOC). Then, the pack temperature could be kept approximately constant during the Cruise (CR) phase until Top Of Descent (TOD), aiming to exploit the thermal inertia of the battery during the descent phase, thus avoiding any heating requirement. If such procedure is implemented, the main operating points characterizing the TMS operating envelope are TO, TOC, CR, and TOD. The cooling requirement during fast-charging is disregarded in this study, as it is assumed that the battery pack is cooled by means of a ground-based system during this phase. A time-dependent heat transfer analysis has been performed to compute the cooling requirements of the battery pack and the EPU at the prescribed operating points at ISA conditions and in presence of very hot weather. The results are reported in Tab. 2. As one can notice, the TMS cooling requirements are only marginally affected by the changes in environmental conditions. This is due to the choice of materials, battery module design, and the type of integration of the battery pack within the wingbox and of the EPU within the engine nacelle.
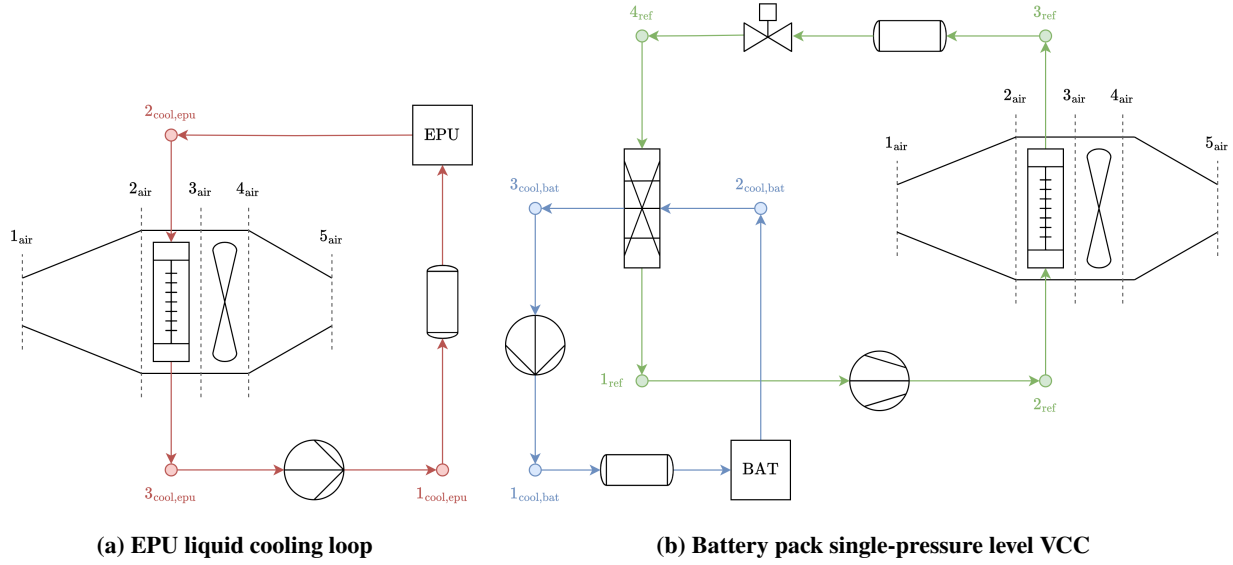
(a) EPU liquid cooling loop   (b) Battery pack single-pressure level VCC

Fig. 3   Baseline TMS architecture, featuring two decoupled cooling loops for the battery pack and the EPU.

IV. System Architectures

Two TMS architectures are assessed and compared in this study. The baseline architecture features two separate cooling loops for the battery pack and the EPU, whereas the alternative TMS configuration exploits the synergy between the two heat sources operating at different temperatures.

A. Baseline Architecture

The baseline TMS configuration for the EPU is a ram air-cooled liquid/oil loop, see Fig. 3a. The working fluid can be either a mixture of water and ethylene/propylene glycol, or a synthetic lubro-refrigerant, such as MIL-PRF-23699. A water-glycol mixture features superior thermodynamic properties, but it cannot be used as lubricant in case a gearbox is present. The main drawback associated with the use of lubro-refrigerants is the sharp increase of their viscosity at temperatures close to 0°C, which in turn complicates the start-up procedure in cold environments. In this work, the selected working fluid is a mixture of water and ethylene glycol with a 50% mass fraction and a mass flow rate of 2 kg/s.

The baseline architecture for the battery pack TMS is a single-pressure level VCC using ram air as heat sink, as displayed in Fig. 3b. Differently from the EPU, whose maximum coolant operating temperature can exceed 100°C, the battery pack TMS cannot rely on a simple ram air-cooled liquid loop. This is due to operating scenarios in which the maximum nominal operating temperature of the battery pack, e.g., 45°C, is lower than the temperature of the heat sink, such as during TO at ISA+35. In such conditions, a heat pump is required. Following previous research on the environmental control system of more electric aircraft [19], the configuration analyzed in this work features a high-speed oil-free centrifugal compressor as prime mover of the VCC. The working fluid of the battery coolant loop is a water-ethylene glycol mixture with a 10% mass fraction and a mass flow rate of 1.5 kg/s, whereas the one used in the refrigerant loop is R1234yf, i.e., a low-GWP replacement for R134a. The influence of the thermophysical properties of different refrigerants on the performance of the VCC is not addressed in this work, but it will be investigated as part of a follow-up study.

B. Alternative Architecture

The alternative TMS architecture is schematically displayed in Fig. 4. The two key features of this configuration are: i) integration of the heat rejection system of the two cooling loops, i.e., condenser and subcooler, in the same ram air duct; ii) coupling of the battery and EPU cooling loops by means of a plate heat exchanger and a bypass system activated by a network of three-way valves. The first feature is enabled by the difference in the operating temperatures of the two heat sources, which directly influence the temperature levels of the two cooling loops. In a nutshell, the same ram air flow that is used as heat sink for the condenser of the VCC can be re-used, despite the temperature rise, as heat

5

sink for the subcooler of the EPU cooling loop. On the one hand, such configuration increases the pressure drop in the ram air duct due to the presence of two heat exchangers in series on the air side. On the other hand, it promotes a higher heat addition in the ram air flow, which ultimately leads to a higher thrust generation in the nozzle due to the Meredith effect [20]. By carefully designing the two heat exchangers, as well as the intake, diffuser and nozzle, it is possible to partially or, in some specific cases, totally offset the drag generated within the ram air duct by exploiting the Meredith effect. Moreover, sharing the same ram air duct for the battery pack and EPU cooling loops promotes a reduction of the detrimental impact of the TMS on the external aerodynamics of the aircraft. The second feature of the alternative TMS architecture allows to use the battery pack as a heat sink for the EPU cooling loop in place of the ram air stream at some designated operating points. Such technological solution has been previously investigated in the context of eVTOLs, as it enables the cooling system of the electric motors and inverters to be downsized for the peak power phase characterized by short transients, i.e., vertical take-off. On the contrary, for large battery-electric aircraft characterized by higher battery capacity and lower C-rate throughout the flight mission, the coupling of the battery and EPU cooling loops can be used to preheat the battery pack during cruise in cold weather, thus ensuring that the battery temperature stays within the nominal range during low-power descent without the need of active heating.
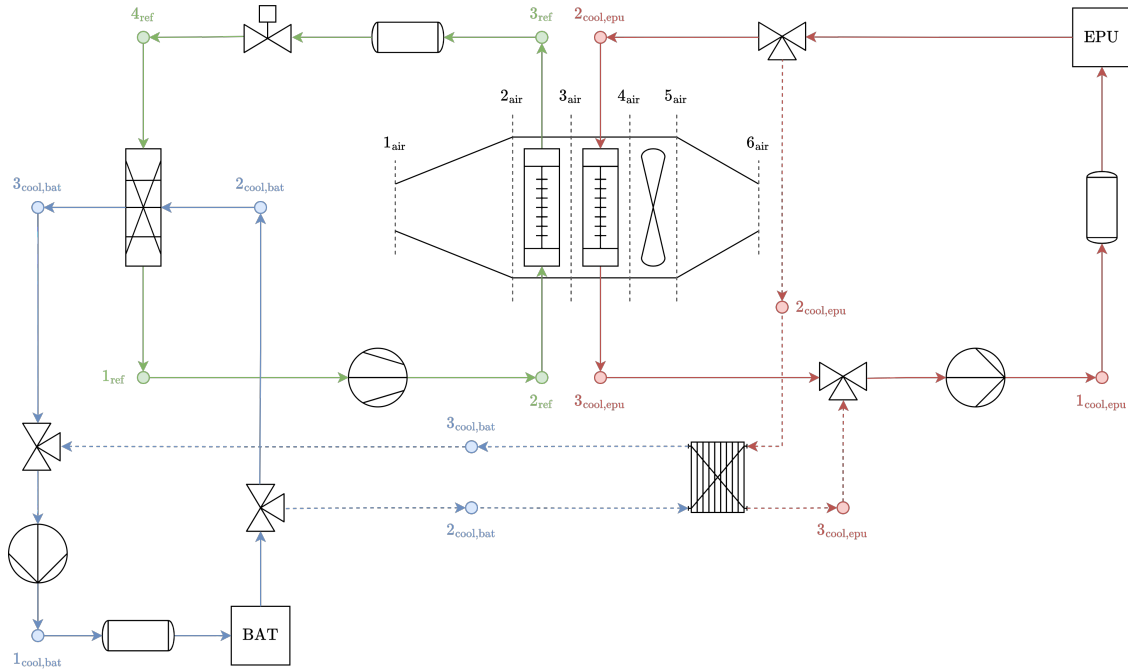

Fig. 4 Alternative TMS architecture, integrating the heat rejection system of the cooling loops for the battery pack and EPU in the same ram air duct. The bypass system coupling the two cooling loops is shown by the dashed lines.

V. Methodology

The models of the baseline and alternative TMS configurations have been implemented in the Modelica language, using the DeSimECS (Design and Simulation of Energy Conversion Systems) library developed by the Propulsion and Power group of Delft University of Technology. All the components are modeled as steady-state and zero-dimensional. The only exceptions are the centrifugal compressor and the evaporator included in the VCC. The former is modeled by means of TurboSim, i.e., a validated Python software developed by the author and documented in [21, 22]. The model combines the lumped parameters approach with one-dimensional flow discretization along key compressor components, and resorts to a blend of physics-based and semi-empirical loss models derived from experimental data. The model is complemented with a method for preliminary weight estimation that accounts for the weight of the compressor assembly by means of a parametric CAD model generated via CadQuery [23], and for the weight of the electric motor by computing its power density with the method documented in [24]. The use of a centrifugal compressor in place of a
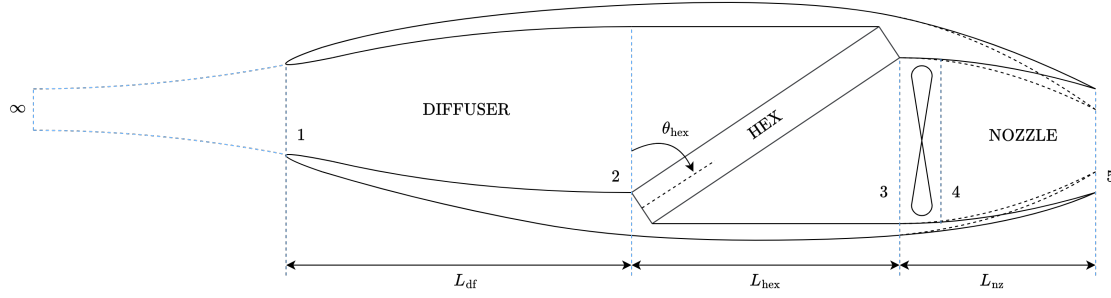
Fig. 5   Ram air duct configuration featuring scoop intake, diffuser, inclined heat exchanger, puller fan, and variable area nozzle.

volumetric machine as prime mover of the VCC leads to significant weight and space savings. Moreover, the use of gas bearings prevents the risk of oil contamination in the refrigerant loop. The topology selected for the evaporator of the VCC is that of gasketed chevron plate. The main advantage of this topology is the high heat transfer coefficient due to the flow turbulence promoted by the corrugations between adjacent plates, which leads to very compact heat exchanger designs. On the downside, this topology is not suitable in presence of high fluid pressure, i.e., $P > 15$ bar, due to leakage issues. However, the evaporator is located in the low-pressure side of the VCC refrigerant loop and the maximum coolant pressure dictated by the battery pack requirements is significantly lower than the aforementioned threshold. The sizing and the performance assessment of the evaporator, including weight estimation, are performed by resorting to the commercial software ASPEN Exchanger Design and Rating, which implements a one-dimensional flow discretization according to the finite volume method. The condenser of the VCC and the subcooler of the EPU cooling loop share the same topology. It consists of alternate flat tubes with an internal microchannel structure and multi-louvered fins brazed on the external surface. The air and the liquid coolant flow according to an unmixed cross-flow arrangement. The liquid flows through the microchannels, whereas the air flows through the passages created by the fins, which are used to extend the heat transfer surface without increasing the volume occupied by the heat exchanger. This topology is typically employed for automotive applications, due to its high compactness. The model of the condenser is extensively described in [19], thus its details are omitted here for brevity. It is implemented according to the moving boundary approach, i.e., the condenser is divided into a number of control volumes equal to the number of working fluid phases: desuperheating (superheated vapor), condensing (liquid-vapor in thermodynamic equilibrium), and subcooling (subcooled liquid). This approach allows for the selection of the most suited correlations for the calculation of the heat transfer coefficient and the pressure drop for each phase [25]. The condenser model has been adapted to describe the subcooler by simply using one control volume representing the subcooled liquid phase. The dry weight of the condenser and the subcooler is directly computed as the product of the density of the selected material and the volume occupied by the flat tubes and fins, multiplied by an empirical coefficient to account for the presence of the casing, manifold, and soldering. Moreover, the weight of the two heat exchangers is increased to account for the presence of liquid coolant or phase-changing refrigerant in the flat tubes. The circulation pump is simply treated as a turbomachinery component featuring a constant isentropic efficiency of $\eta_{is} = 55\%$. The pump weight is estimated separately by selecting a component from the catalogue of a commercial supplier that meets the requirements expressed in terms of head and volumetric flow rate. The coolant pipes are sized to ensure that the coolant velocity does not exceed 3 m/s in any part of the circuit. The estimated pipe length is 4 meters and 10 meters for each EPU and battery cooling circuit, respectively; the weight estimation accounts for both the solid and fluid sections of the pipe.

The ram air duct is constituted by five components in series, i.e., intake, diffuser, heat exchanger, fan, and a nozzle featuring variable geometry, as displayed in Fig. 5. In the case of the alternative TMS configuration, the ram air duct features six components, as the condenser and the subcooler are placed in series. In this work, a scoop intake with elliptical shape is adopted, and is modeled according to the methodology documented in [26]. The drag penalty associated with the intake can be expressed as

$$D = \dot{m}_\infty v_\infty \frac{C_D}{2} \tag{1}$$

where $\dot{m}_\infty$ is the ideal mass flow processed by the intake in free-stream conditions

$$\dot{m}_\infty = \rho_\infty v_\infty A \tag{2}$$

and C_D is the drag coefficient. This is expressed as the sum of the ram drag coefficient, the skin friction drag coefficient, the spillage drag coefficient, and two corrections accounting for the presence of a diverter, and the increase of drag at values of mass flow rate close to the choking point of the intake. These coefficients are evaluated with the semi-empirical correlations reported in [26]. The pressure recovery factor of the intake is expressed as

$$C_p = \frac{P_{t,1} - P_\infty}{P_{t,\infty} - P_\infty}, \tag{3}$$

where $P_{t,\infty}$ and P_∞ refer to the total and static pressure at free-stream conditions. The pressure recovery factor is evaluated with a series of semi-empirical correlations in the same fashion as the drag coefficient. The static pressure recovery in the diffuser is interpolated from the experimental data for two-dimensional rectangular diffuser reported in [27]. Notably, this methodology introduces some modeling uncertainties, as the actual diffuser geometry might deviate from the two-dimensional rectangular shape. The heat exchanger(s) is placed at a non-zero angle θ with respect to the flow direction, in order to reduce the overall dimensions of the ram air duct, thus its impact on the external aircraft aerodynamics. However, this increases the pressure drop across the heat exchanger(s) on the ram air side, and it may lead to flow maldistribution in case the inclination angle is excessive. In this work, θ is limited up to 60°, and the increase in pressure drop is estimated with the empirical method documented in [28]. The presence of a ram air fan is needed when the pressure drop across the heat exchanger(s) is higher than the static pressure recovery in the intake and the diffuser. This scenario is usually associated with low aircraft speed and high ram air mass flow rate requirement, such as during TO in a hot environment. Throughout the remainder of the flight mission, the ram air fan could be de-activated to reduce the electric power consumption. However, even if not active, the presence of the fan within the ram air duct introduces additional weight and pressure losses due to wind-milling. Therefore, the design of low-pressure drop heat exchanger(s) and high-pressure recovery intake and diffuser, such to avoid the need for a ram air fan, could enable a sizeable improvement of the ram air duct performance. In this work, the ram air fan is treated as a turbomachinery component featuring a constant isentropic efficiency of $\eta_{is} = 65\%$, and it is activated only when the total pressure at the heat exchanger outlet falls below the free-stream static pressure augmented by 1 kPa. When the fan is not active, the pressure drop associated to wind-milling is neglected for simplicity. The weight of the ram air fan and its motor is estimated with the empirical fitting proposed in [29]

$$m_{fan} = 0.3 \cdot 7.022 \dot{m}_{air} + 0.889 \cdot \left(\frac{P_{el}}{1000}\right)^{0.9} \tag{4}$$

The nozzle is placed downstream of the ram air fan, and is used to offset part of the drag penalty associated with the intake by expanding the energized ram air flow, thus generating thrust. The nozzle outflow area is actively adjusted by means of actuators, to match the ram air mass flow rate requirement in each operating point. The model of the nozzle follows the methodology described in [30]. The net drag force generated by the ram air duct is computed as

$$D_{net} = D_{intake} - T_{nozzle} \tag{5}$$

VI. Results and Discussion

The ram air duct of the two TMS architectures, including the condenser and subcooler, is sized at the most critical operating point, i.e., TO ISA+35. Notably, the condenser is sized at TO ISA+35, even though the maximum cooling requirement associated with the battery pack is at TOC ISA+35, as reported in Tab. 2. Indeed, the highest temperature of the heat sink is measured at TO ISA+35, therefore leading to the maximum ram air flow requirement, which in turn sizes the frontal area and the finned passages of the condenser. Both the condenser and the subcooler feature a frontal area of 0.446 m^2 and a porosity of about 0.94, defined as $\phi = 1 - V_{ht}/V$, where V_{ht} is the total metal volume used for heat transfer, and V is the geometrical volume calculated with the outer heat exchanger dimensions. The maximum pressure drop calculated at TOC ISA+35 across the two heat exchangers on the air side is 1.02 kPa for the condenser and 1.19 kPa for the subcooler. On the contrary, the evaporator is sized for the maximum battery cooling requirement at TOC ISA+35. The selected evaporator design features 21 M6 plates from the manufacturer Alfa Laval. The maximum temperature lift of the VCC, hence the maximum pressure ratio that must be provided by the refrigerant compressor, is required at TO ISA+35 to achieve a sufficient temperature difference between the heat sink and the refrigerant stream without requiring
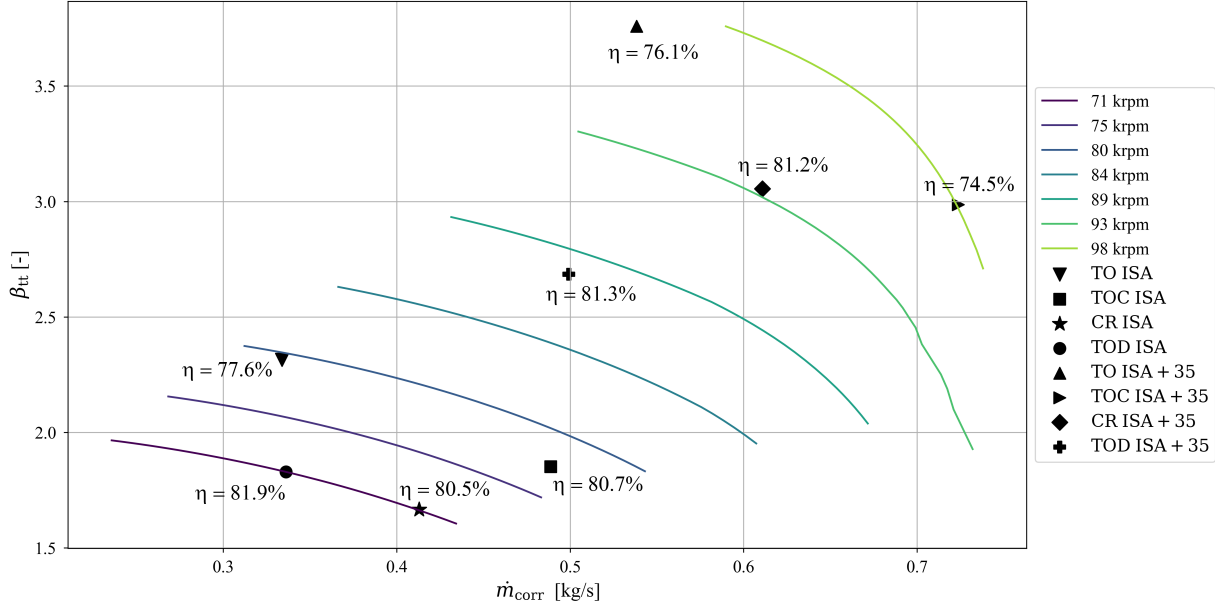
Fig. 6 Operating map of the refrigerant compressor powering the VCC system of the alternative TMS architecture.

an excessive heat transfer area of the condenser. The operating map of a centrifugal compressor preliminary sized using TurboSim for the alternative TMS configuration is displayed in Fig. 6. The selected compressor design features a design rotational speed of about 90,000 rpm, an impeller inlet and outer diameter of 15.2 mm and 40.6 mm, respectively, and an impeller back-sweep angle of 48°. The maximum power and torque specifications for the design of the electric motor are 19.5 kW and 1.91 Nm obtained at around 98,000 rpm. As one can notice in Fig. 6, a high-speed single-stage compressor can effectively cover all the operating points of the VCC with a calculated total-to-total isentropic efficiency in between 75% and 82%. As expected, the most stringent operating condition is defined by TO ISA+35, due to the combination of maximum pressure ratio and lower mass flow rate as compared to TOC ISA+35 and CR ISA+35. To achieve higher efficiency and guarantee stable compressor operation at such condition, the design can be further refined using automated optimization methods and higher fidelity tools; however, this is outside the scope of the present work.

Once the main components of the TMS have been sized, the off-design performance of the two proposed system configurations have been evaluated. The main results computed for the baseline and alternative TMS architectures are summarized in Tab. 3 and Tab. 4, respectively. Notably, the electric power consumption of the two TMS configurations is almost equal across the operating points at ISA conditions, whereas it shows up to ≈ 15% change at ISA+35. The power consumption is mostly driven by the refrigerant compressor, and, in turn, by the temperature lift provided by the VCC. Therefore, when the refrigerant compressor operates at the same pressure ratio, the power consumption of the two system configurations is almost identical. This holds for most of ISA conditions, but not for ISA+35, as the ram air intake of the VCC of the baseline architecture is slightly downsized, thus leading to variations in the temperature lift requirement at high temperatures of the heat sink. Furthermore, the alternative TMS architecture shows a consistent reduction of the net drag penalty across all the prescribed operating points. This is largely due to a reduction of the external drag, here defined as the component of the drag penalty associated with the disturbance of the external aerodynamic flow induced by the presence of the intake(s), such as, e.g., the spillage drag. The decrease in external drag is simply achieved by placing the condenser and the subcooler in the same ram air duct, thus reducing the total frontal area of the intake(s) and the wetted surface area of the ram air duct(s). To conclude the comparison, the total weight of the two systems have been computed accounting for the presence of eight EPUs and eight battery packs distributed along the wing; the result is equal to 1282 kg and 1130 kg for the baseline and the alternative configuration, respectively. The weight penalty of the baseline architecture is due to the duplication of the ram air duct components, i.e., intake, diffuser, fan, and nozzle.

The thermodynamic principle that enables the operation of the two heat exchangers in series using the same heat sink is schematically explained in Fig. 7. The chart shows only the operating points at ISA conditions for the sake of

9

Table 3 Key performance metrics of the baseline TMS architecture computed at the operating points defined in Tab. 2. The values of drag and power consumption refer to eight EPUs and battery packs, whereas the values of air mass flow rate refer to one ram air duct.

Operating Point	P_{el} [kW]	D_{net} [N]	D_{ext} [N]	$\dot{m}_{air,bat}$ [kg/s]	$\dot{m}_{air,epu}$ [kg/s]
TO ISA	64.9	488	1225	1.80	1.10
TOC ISA	69.4	1165	3677	1.55	0.94
CR ISA	51.8	1252	3597	1.36	0.90
TOD ISA	37.6	1279	3565	1.28	0.90
TO ISA+35	211.9	1528	335	3.60	2.18
TOC ISA+35	206.7	1459	3724	2.57	1.11
CR ISA+35	160.1	1479	3775	2.44	1.19
TOD ISA+35	121.4	1367	3844	2.08	1.19

Table 4 Key performance metrics of the alternative TMS architecture computed at the operating points defined in Tab. 2. The values of drag and power consumption refer to eight EPUs and battery packs, whereas the values of air mass flow rate refer to one ram air duct.

Operating Point	P_{el} [kW]	D_{net} [N]	D_{ext} [N]	$\dot{m}_{air}$ [kg/s]
TO ISA	64.9	378	833	1.80
TOC ISA	69.4	842	2486	1.55
CR ISA	51.8	912	2418	1.36
TOD ISA	27.6	926	2440	1.42
TO ISA+35	239.7	1012	243	3.80
TOC ISA+35	176.5	1602	2460	2.83
CR ISA+35	141.1	1474	2496	2.69
TOD ISA+35	105.5	1216	2602	2.32

clarity; however, the same principle is applicable to the entire operating envelope. First, the ram air stream enters the condenser at low temperature and is used as heat sink to achieve full condensation of the refrigerant stream. The air temperature rise is controlled by three parameters: i) condensation pressure; ii) degree of subcooling; iii) ram air mass flow rate. Then, the same ram air stream is conveyed to the subcooler and is further heated until the target EPU coolant temperature is achieved. As briefly mentioned in Section IV, the enthalpy increase in the ram air flow induced by the heat transfer can partially, and, in some specific cases, totally offset the additional pressure drop generated in the ram air duct due to the presence of two heat exchangers in series, thanks to the Meredith effect. It is important to highlight that, as the two heat exchangers feature a cross-flow configuration, the ram air outlet temperature defines the theoretical minimum temperature that can be obtained in the EPU coolant stream. To reduce this temperature, one needs to increase the heat capacity of the ram air stream, i.e., increase the ram air flow rate, thus leading to a reduction of the slope of the blue lines in Fig. 7. However, this typically leads to an increase of pressure drop across the heat exchangers at fixed frontal area and possibly to an oversizing of the intake. In light of the above, the correct functioning of the alternative TMS architecture is enabled by the fine tuning of the VCC operation, and of the ram air mass flow rate, by means of an active control of the nozzle outflow area, as well as by the difference in the maximum nominal operating temperature of the two heat sources.

To further assess the performance improvement enabled by the alternative TMS architecture, it is possible to convert the drag penalty and electric power consumption into an equivalent battery mass that must be carried onboard the aircraft
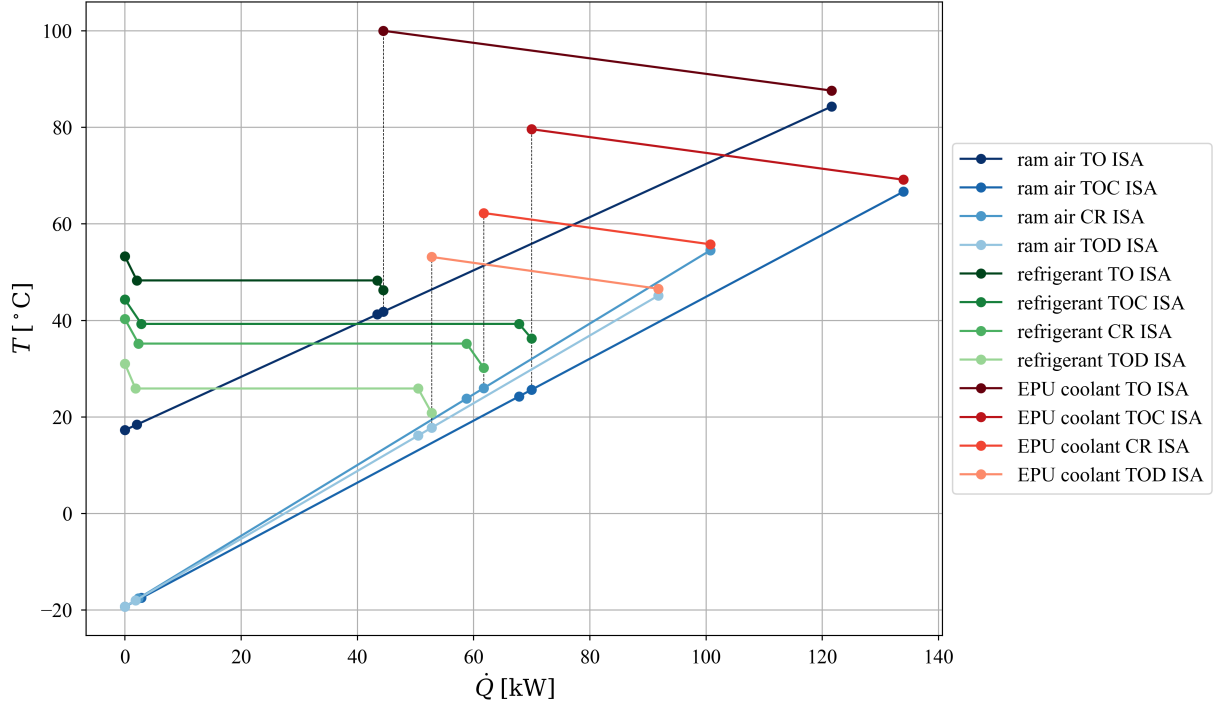
Fig. 7   Temperature - heat flow rate diagram for the ram air duct of the alternative TMS architecture operating at ISA conditions.

to enable the operation of the TMS. In particular, the equivalent battery mass due to the drag penalty can be computed as

$$m_{D,\text{eq}} = \int \frac{D v_\infty}{\eta_\text{p} \eta_\text{pmad} \eta_\text{bat}} dt, \tag{6}$$

whereas the one due to the electric power consumption reads as follows

$$m_{P,\text{eq}} = \int \frac{P_\text{el}}{\eta_\text{bat}} dt \tag{7}$$

The integrals in Eqn. (6) and Eqn. (7) are computed considering the nominal mission flown at ISA conditions, as the battery mass is sized for such scenario. The reserve mission is disregarded for simplicity in this analysis, even though the target aircraft is designed such that the go-around and initial climb phases are flown on battery power to allow for the start-up of the reserve energy system. The propulsion system operates close to idle conditions during the descent phase, hence the heat generation in the electric powertrain is close to zero. Therefore, only the electric power consumption due to the coolant pumps and the aerodynamic penalty due the spillage drag induced by the presence of partially closed intakes are considered during the descent phase. The sum of the TMS mass and the equivalent battery mass computed with Eqn. (6) and Eqn. (7) is equal to 2351 kg and 1963 kg for the baseline and alternative architecture, respectively. To complement this analysis, a detailed breakdown of the various weight contributions is reported in Fig. 8 for the alternative TMS configuration. The results show that, by integrating the condenser and subcooler in the same ram air duct, the alternative TMS architecture leads to an equivalent total weight savings of 388 kg. If such a weight budget is allocated for the installation of additional batteries, the resulting increase in usable range can be computed using the modified Breguet range equation [31]

$$\Delta R_\text{max} = \eta_\text{bat} \eta_\text{pmad} \eta_\text{p} e_\text{us} \frac{1}{g} \left(\frac{L}{D} \right)_\text{max} \left(\frac{\Delta \text{EM}}{\text{MTOM}} \right), \tag{8}$$

leading to $\Delta R_\text{max} = 11$ km. This calculation is valid under the assumption that the energy carried by the additional battery mass is used to extend the cruise phase, without altering the excess energy used for taxiing, take-off, go-around,
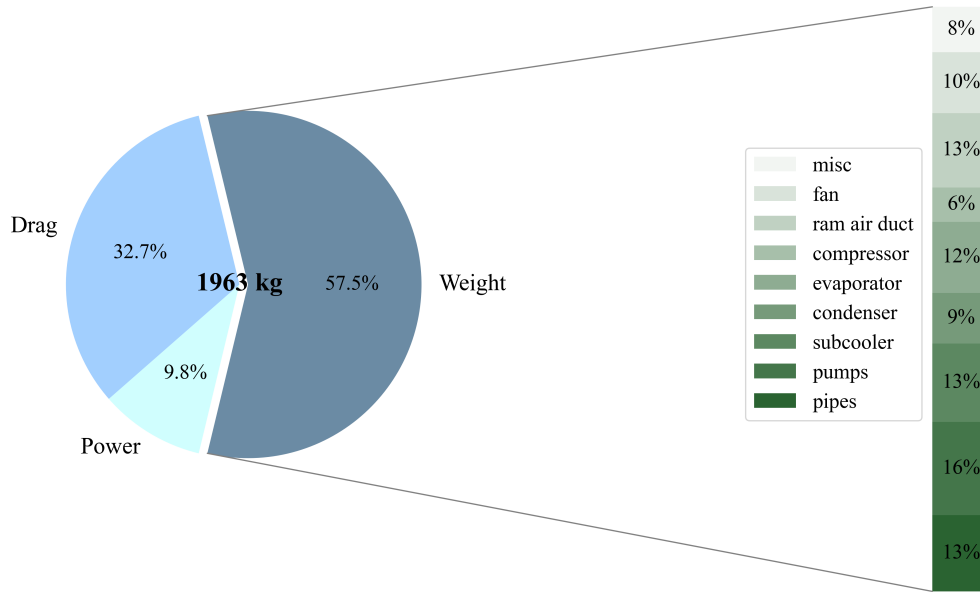
11

Fig. 8 Equivalent battery mass required for the alternative TMS architecture, split into the quotas due to system weight, drag penalty, and electric power consumption. The weight contribution is further split into individual components.

and to compensate for the inefficiencies during climb and diversion climb. Moreover, this calculation does not account for any snowball effect.

VII. Conclusion

The preliminary design of two different TMS architectures for the electric powertrain of a 90-seater battery-powered aircraft has been addressed in this work. The baseline configuration features a mechanically pumped liquid cooling loop for the EPU, and a single-pressure level VCC for the battery pack, both using ram air as heat sink. The alternative configuration exploits the difference in the maximum nominal operating temperature of the two heat sources by integrating the heat rejection system of the two cooling loops, i.e., condenser and subcooler, in the same ram air duct. The main components of the two systems, i.e., condenser, evaporator, subcooler, and refrigerant compressors, have been sized at the most critical operating point, and the off-design performance of the two configurations have been evaluated at various operating points throughout the flight mission. The main take-aways can be summarized as follows:

- the alternative TMS configuration achieves lower weight and drag penalty by reducing the total number of ram air ducts, thus minimizing the perturbation of the aircraft external aerodynamics;
- the additional pressure drop generated within the ram air duct due to the presence of two heat exchangers in series is partially, and, in some cases, totally offset by the Meredith effect;
- the alternative TMS configuration leads to a savings of equivalent battery mass in the order of 388 kg, promoting an increase in the usable range of 11 km prior to snowball effects.

Future work will assess the performance gains achievable by adopting a more complex TMS configuration, such as a multi-pressure level VCC, as well as by optimizing the thermodynamic cycle parameters together with the working fluid selection. Moreover, future studies will focus on the operating conditions where the cooling circuits of the battery pack and EPU can be coupled by means of the bypass system briefly described in this work.

References

[1] Ritchie, H., Roser, M., and Rosado, P., "Energy," *Our World in Data*, 2022. Https://ourworldindata.org/energy.

[2] Advisory Council for Aviation Research and Innovation in Europe (ACARE), "Realising Europe's vision for aviation: Strategic research & innovation agenda, Vol. 1," Advisory Council for Aviation Research and Innovation in Europe, 2012.

[3] for Aviation Research, A. C., and in Europe (ACARE), I., "Strategic Research and Innovation Agenda," Advisory Council for Aviation Research and Innovation in Europe, 2017.

[4] Mukhopadhaya, J., and Graver, B., "Performance Analysis of Regional Electric Aircraft," International Council of Clean Transportation white paper, 2022.

[5] Staack, I., Sobron, A., and Krus, P., "The potential of full electric aircraft for civil transportation: from the Breguet range equation to operational aspects," *CEAS Aeronautical Journal*, Vol. 12, 2021, pp. 803–819. https://doi.org/10.1007/s13272-021-00530-w.

[6] Webber, H., and Job, S., "Realising Zero-Carbon Emission Flight," Aerospace Technology Institute report FZ-0-6.1, September 2021.

[7] Epstein, A. H., and O'Flarity, S. M., "Considerations for Reducing Aviation's CO_2 with Aircraft Electric Propulsion," *Journal of Propulsion and Power*, Vol. 35(3), 2019, pp. 572–582. https://doi.org/10.2514/1.B37015.

[8] Wolleswinkel, R. E., de Vries, R., Hoogreef, M., and Vos, R., "A New Perspective on Battery-Electric Aviation, Part I: Reassessment of Achievable Range," *AIAA SciTech Forum*, American Institute of Aeronautics and Astronautics, 2024. https://doi.org/10.2514/6.2024-1489.

[9] de Vries, R., Wolleswinkel, R. E., Hoogreef, M., and Vos, R., "A New Perspective on Battery-Electric Aviation, Part II: Conceptual Design of a 90-Seater," *AIAA SciTech Forum*, American Institute of Aeronautics and Astronautics, 2024. https://doi.org/10.2514/6.2024-1490.

[10] de Vries, R., Brown, M., and Vos, R., "Preliminary Sizing Method for Hybrid-Electric Distributed-Propulsion Aircraft," *Journal of Aircraft*, Vol. 56, No. 6, 2019, pp. 2172–2188. https://doi.org/10.2514/1.C035388.

[11] Finger, D. F., de Vries, R., Vos, R., Braun, C., and Bil, C., "Cross-Validation of Hybrid-Electric Aircraft Sizing Methods," *Journal of Aircraft*, Vol. 59, No. 3, 2022, pp. 742–760. https://doi.org/10.2514/1.C035907.

[12] Affonso, W., Tavares, R. T., Barbosa, F. R., Gandolfi, R., dos Reis, R. J. N., da Silva, C. R. I., Kipouros, T., Laskaridis, P., Enalou, H. B., Chekin, A., Kukovinets, A., Gubernatorov, K., Ravikovich, Y., Ivanov, N., Ponyaev, L., and Holobtsev, D., "System architectures for thermal management of hybrid-electric aircraft - FutPrInt50," *IOP Conference Series: Materials Science and Engineering*, Vol. 1226, No. 1, 2022, p. 012062. https://doi.org/10.1088/1757-899X/1226/1/012062.

[13] Rheaume, J., and Lents, C. E., "Design and Simulation of a Commercial Hybrid Electric Aircraft Thermal Management System," *AIAA/IEEE Electric Aircraft Technologies Symposium (EATS)*, 2018. https://doi.org/10.2514/6.2018-4994.

[14] Rheaume, J. M., Macdonald, M., and Lents, C. E., "Commercial Hybrid Electric Aircraft Thermal Management System Design, Simulation, and Operation Improvements," *AIAA/IEEE Electric Aircraft Technologies Symposium (EATS)*, 2019, pp. 1–23. https://doi.org/10.2514/6.2019-4492.

[15] Kellermann, H., Lüdemann, M., Pohl, M., and Hornung, M., "Design and Optimization of Ram Air–Based Thermal Management Systems for Hybrid-Electric Aircraft," *Aerospace*, Vol. 8, No. 1, 2021. https://doi.org/10.3390/aerospace8010003.

[16] Planès, T., Habrard, V., Delbecq, S., Pommier-Budinger, V., and Benard, E., "Thermal management system models for overall aircraft design," *AIAA Aviation Forum*, American Institute of Aeronautics and Astronautics, 2021. https://doi.org/10.2514/6.2021-2428.

[17] de Vries, R., Wolleswinkel, R., Rosen Jacobsen, D., Bonnema, G., and Thiede, S., "Battery Performance Metrics for Large Electric Passenger Aircraft," *34th Congress of the International Council of Aeronautical Sciences (ICAS)*, 2024.

[18] Rheaume, J. M., and Lents, C. E., "Commercial Hybrid Electric Aircraft Thermal Management Sensitivity Studies," *AIAA/IEEE Electric Aircraft Technologies Symposium (EATS)*, 2020, pp. 1–6.

[19] Giuffré, A., Ascione, F., Colonna, P., and De Servi, C., "Integrated Design Optimization of Environmental Control Systems for Next-Generation Aircraft," *Journal of Aircraft*, 2025. https://doi.org/10.2514/1.C038093.

[20] Meredith, F. W., "Cooling of aircraft engines with special reference to ethylene glycol radiators enclosed in ducts," Tech. rep., Aeronautical Research Committee, 1935.

13

[21] Giuffré, A., Colonna, P., and Pini, M., "The Effect of Size and Working Fluid on the Multi-Objective Design of High-Speed Centrifugal Compressors," *International Journal of Refrigeration*, Vol. 143, 2022, pp. 43–56. https://doi.org/10.1016/J. IJREFRIG.2022.06.023.

[22] Giuffré, A., Colonna, P., and Pini, M., "Design Optimization of a High-Speed Twin-Stage Compressor for Next-Gen Aircraft Environmental Control System," *Journal of Engineering for Gas Turbines and Power*, Vol. 145, No. 3, 2023. https://doi.org/10.1115/1.4056022.

[23] Kirkby, S., Buchanan, J., Wright, J., Boin, P., Urbanczyk, A., and Boyd, M., "CadQuery, Release 2," , 2022. URL https://github.com/CadQuery/cadquery/.

[24] Van Der Geest, M., Polinder, H., Ferreira, J. A., and Christmann, M., "Power density limits and design trends of high-speed permanent magnet synchronous machines," *IEEE Transactions on Transportation Electrification*, Vol. 1, No. 3, 2015, pp. 266–276. https://doi.org/10.1109/TTE.2015.2475751.

[25] Ascione, F., Colonna, P., and De Servi, C., "Integrated design optimization method for novel vapour-compression-cycle-based environmental control systems," *Applied Thermal Engineering*, Vol. 236, 2024, pp. 121–261. https://doi.org/10.1016/j. applthermaleng.2023.121261.

[26] ESDU, *86002: Drag and pressure recovery characteristics of auxiliary air inlets at subsonic speeds*, 2004.

[27] Sovran, G., "Experimentally Determined Optimum Geometries for Rectlinear Diffusers with Rectangular, Conical or Annular Cross Section," *Fluid Mechanics of Internal Flow*, 1967, pp. 270–319.

[28] Nichols, M., "Investigation of flow through an intercooler set at various angles to the supply duct," Tech. rep., NASA Langley Research Center, 1942.

[29] Frey, A. C., Stonham, J., Bosak, D., Sangan, C. M., and Pountney, O. J., "Radiators in fuel cell powered aircraft: the effect of heat rejection on drag," *Applied Thermal Engineering*, Vol. 274, 2025, p. 126697. https://doi.org/10.1016/j.applthermaleng. 2025.126697.

[30] Grey, R., and Wilsted, H., "Performance of conical jet nozzles in terms of flow and velocity coefficients," Tech. rep., NACA Lewis Flight Propulsion Laboratory, 1949.

[31] de Vries, R., Hoogreef, M., and Vos, R., "Range Equation for Hybrid-Electric Aircraft with Constant Power Split," *Journal of Aircraft*, Vol. 57, No. 3, 2020. https://doi.org/10.2514/1.C035734.